



GEOPHYSICS®

Surface-wave dispersion spectrum inversion method applied to Love and Rayleigh waves recorded by DAS

Journal:	<i>Geophysics</i>
Manuscript ID	GEO-2019-0691.R3
Manuscript Type:	Technical Paper
Keywords:	surface wave, distributed systems, dispersion
Manuscript Focus Area:	Engineering and Environmental Geophysics, Seismic Inversion

SCHOLARONE™
Manuscripts

Surface-wave dispersion spectrum inversion method applied to Love and
Rayleigh waves recorded by DAS

Right Running Head: DAS surface-wave dispersion spectrum inversion

Zhenghong Song^{1,2}, Xiangfang Zeng^{2*}, Clifford H. Thurber³

1. School of Earth and Space Sciences, University of Science and Technology of
China, Hefei, 230026, China. E-mail: zhhsong6@mail.ustc.edu.cn.
2. State Key Laboratory of Geodesy and Earth's Dynamics, Innovation Academy
for Precision Measurement Science and Technology, Chinese Academy of Sciences,
Wuhan, 430077, China. E-mail: zengxf@apm.ac.cn
3. Department of Geoscience, University of Wisconsin-Madison, Madison, WI 53706,
USA. E-mail: cthurber@wisc.edu

*corresponding author: zengxf@apm.ac.cn

Abstract:

Recently, Distributed Acoustic Sensing (DAS) has been applied to shallow seismic structure imaging providing dense spatial sampling at a relatively low cost. DAS on a standard straight fiber-optic cable mostly records axial dynamic strain, which makes it difficult to separate Rayleigh and Love wavefields. As a result, the mixed Rayleigh and Love wave signals cannot be used in the conventional surface-wave dispersion inversion method. Therefore, it is often ensured that the source and the cable are in the same line and only Rayleigh wave dispersion is used, which limits constraints on structure and model resolution. We propose to invert surface wave dispersion spectra instead of dispersion curves. This inversion method can use mixed Rayleigh and Love waves recorded when the source and receiver array are not aligned. The multiple-channel records are transformed to the frequency domain and a slant stack method is used to construct the dispersion spectra. The genetic algorithm method is employed to obtain an optimal S-wave velocity model that minimizes the difference between theoretical and observed dispersion spectra. A series of synthetic tests are conducted to validate our method. The results suggest that our method not only improves the flexibility of the acquisition system design, but the Love wave data also provide additional constraints on the structure. Our method is applied to the active source and ambient noise datasets acquired at a geothermal site and provides consistent results for different datasets and acquisition geometries. The sensitivity of the dispersion spectra to layer thickness, density and P-wave velocity is also discussed. With our method, the amount of usable data can be increased, helping to deliver better subsurface images.

INTRODUCTION

Knowledge of the shallow seismic velocity structure (especially S-wave) is important for ground motion simulation, underground space utilization, and other seismological studies such as tomography and earthquake locations (e.g., Borchardt, 1994; Li et al., 2014; Ahmadi and Eskandari., 2014; Eskandari et al., 2014; Eskandari et al., 2017; Ai et al., 2018). Surface wave imaging methods, including active source and passive source methods, are widely used to image shallow S-wave velocity structure (e.g., Foti et al., 2011). Since the higher frequency surface wave is more sensitive to the shallower structure, a dense acquisition system is needed to avoid wavefield aliasing. For a city-wide scale study, thousands of observation sites are needed and it is expensive and time consuming using standard seismic instruments (e.g., Lin et al., 2013).

Recently, a new seismic acquisition technique known as Distributed Acoustic Sensing (DAS) was introduced to the seismology community and successfully used in borehole observations (e.g., Mateeva et al., 2017; Zhan, 2020), earthquake monitoring (e.g., Lindsey et al., 2017), and seismic tomography (e.g., Parker et al., 2018). One advantage of DAS is the small channel spacing (1-10 meters) that can be achieved at relatively low cost, especially if existing (dark) fiber-optic cable is available. Previous studies show that high-frequency active and passive-source surface-wave signals recorded with DAS can be used to image shallow seismic structure (Dou et al., 2017; Zeng et al., 2017a; Song et al., 2018).

As is well known, DAS is mostly sensitive to axial (along cable) dynamic strain

or strain rate that is effectively equivalent to a single component sensor (e.g., Parker et al., 2014; Kuvshinov, 2016). The surface wave dispersion curve extracted from active or passive sources is typically used to invert for a layered model beneath the cable (e.g., Dou et al., 2017; Zeng et al., 2017a) with pure Rayleigh or Love wave records (Figure 1a, the inline case). In many cases, however, the source is not in-line with the cable and the records include contributions from both Rayleigh and Love waves (Figure 1b, the crossline case), hampering the ability to properly model the data. Since the Rayleigh and Love waves have different polarizations, rotation is one of the most popular approaches to separate Rayleigh and Love waves signals when two orthogonal horizontal components are available. A solution for this challenge for DAS is recording more components of strain tensors with specially designed cable (e.g., Ning and Sava, 2018) or array geometry (e.g., Innanen et al., 2019), which significantly increases deployment cost and is not an option for dark fiber.

In addition to dispersion curve inversion, another family of methods for inverting surface wave spectra has been introduced to overcome difficulties in dispersion curve construction and mode identification (e.g., Forbriger, 2003; Ryden and Park, 2006; Maraschini et al., 2010; Maraschini and Foti, 2010; Dou and Ajo-Franklin, 2014). These methods transform the time-domain wavefield into frequency-phase velocity-domain dispersion spectra, and the difference between the observed and theoretical dispersion spectra is used as the objective function for inversion. In this paper, we adopt a similar idea to invert surface wave dispersion spectra instead of dispersion curves, which does not require Rayleigh and Love wave separation. This paper is structured as

follows. First, a series of synthetic tests are conducted to demonstrate the crossline issue and verify our method. Then, our method is applied to a real dataset. We conclude with a discussion of the effect of other factors on this analysis method.

SYNTHETIC TESTS

Forward modeling

In this section, we use a typical frequency range (5-25 Hz) for shallow seismic structure imaging studies (Xia et al., 1999; Foti et al., 2011). The P-wave velocity is derived from S-wave velocity via an empirical relationship, and density is defined as a function of P-wave velocity (Brocher, 2005). As pointed out by Rix et al. (1991), the penetration depth is generally considered to be approximately half the maximum wavelength. However, the penetration depth in practice is more complicated. The first model used in the synthetic tests consists of three 10-m thick layers over a half-space (Table 1, model 1). The hypothetical acquisition system is a 100-m long cable segment with a channel spacing of 1-m. The minimum offset is set to 100-m following the suggestion of Pan et al. (2013). For the crossline case, the azimuth of the source to the minimum offset station is 45° and it is 22.5° at the maximum offset.

The forward modeling for our first set of synthetic tests is based on the modal summation method (Herrmann 2013). The seismic source is a single force imposed on the ground (Figure 1a and 1b) with an impulse source-time function. The receivers are placed on the ground at a 1-m interval and the displacement records for the radial and transverse components at each receiver are computed. The displacement in the cable

direction is obtained as a linear combination of the radial and transverse records. The dynamic strain record (Figure 1c) is computed by applying first order central difference on the displacement records, corresponding to a gauge length of 2-m. In practice, the gauge length can be optimized according to the wavelength of the signal of interest in some commercially available instruments (Dean et al., 2016).

Figures 2a and 2c demonstrate synthetic waveforms for both the inline and crossline cases, respectively, for model 1 (Table 1). As mentioned before, both Rayleigh and Love waves contribute to the DAS record in the crossline case, whereas only the Rayleigh wave emerges in the inline case.

Data processing

Surface-wave dispersion spectra can be obtained with multiple channel records with various transformations (e.g., Henry et al., 1980; McMechan and Yedlin, 1981; Park et al., 1999; Forbriger, 2003). Here, we used a straightforward frequency-domain slant-stack method, as follows:

- (1) Transform from the time domain to the frequency domain with the Fourier transform

$$U(x, f) = \int_{-\infty}^{\infty} d(x, t) e^{-i2\pi f t} dt \quad (1)$$

where $d(x, t)$ is the raw (unnormalized) waveform recorded by a receiver at offset x .

- (2) Compute the phase shift with offset x and assumed phase velocity c

$$ph(x, f) = e^{i2\pi f x/c} \quad (2)$$

(3) stack shifted records in the frequency-phase velocity domain

$$P(c,f) = \int_{x_0}^{x_1} e^{i2\pi fx/c} \left[\frac{U(x,f)}{|U(x,f)|} \right] dx \quad (3)$$

To suppress possible amplitude variation across channels, the amplitude of each trace has been normalized (equation 3). Figures 2b and 2d are the dispersion spectra for the records shown in Figure 2a and 2c, respectively. Obviously, it is impossible to pick the correct Rayleigh/Love wave dispersion curve correctly in the crossline case (Figure 2d).

Inversion

A genetic algorithm is used for inversion (Chipperfield et al., 1994). As a global search method, the genetic algorithm is more reliable for achieving the global minimum and has the capability of sampling a large model space (e.g., Lomax and Snieder, 1994). The initial model is randomly generated in the model space (Table 1). The objective function φ_{obj} is defined as the root-mean-square of the spectral difference:

$$\varphi_{obj} = \sqrt{\frac{\sum_{i=1}^{nf} \sum_{j=1}^{nc} (O_{i,j} - M_{i,j})^2}{nf \cdot nc}}, \quad (4)$$

where nc and nf are the numbers of phase velocities and frequencies, respectively, $O_{i,j}$ is the normalized observed dispersion spectrum, and $M_{i,j}$ indicates the normalized theoretical dispersion spectrum.

We first test the reliability of the dispersion spectrum inversion method for the inline case with synthetic records obtained from model 1 (Table 1). The layer thickness is fixed and we solve for just the S-wave velocities. P-wave velocity and density are obtained with empirical relationships, as noted above. In this favorable case, both the

dispersion curve and dispersion spectrum inversion methods provide suitable results. The dispersion curve inversion result recovers the top two layers well, whereas the bottom layer and the half-space are not well recovered. A possible reason is the larger picking error at lower frequencies compared to the higher frequencies (Figure 3a and 3b). The model obtained with the dispersion spectrum inversion is much closer to the true model, which indicates the dispersion spectra can tighten model constraints via using more information. We test the crossline case with the same model, the inversion result of the crossline case is shown in Figure 4. The input model is well recovered with a small misfit. The average model difference is only 1.01 m/s and the misfit is down to 0.24%. Both are comparable to the inline case (5.2 m/s and 0.75%).

Low-velocity layer test

As pointed out by Dou and Ajo-Franklin (2014), the dispersion spectra inversion can reveal a low velocity layer at depth. In their studies, the acquisition system is similar to our Rayleigh wave only inline case. In our crossline case, the Love wave signal is also used, providing additional constraints. A model with a low velocity layer (model 2 in Table 1) is designed to test this expectation. Compared to the inline case, a stronger lower frequency component emerges in the dispersion spectrum of the crossline case (Figure 5). The low-frequency component is mostly contributed by the Love wave. Since a lower frequency is sensitive to a greater depth, the lack of a low-frequency component for the inline case results in a larger error in the bottom layer and the half-space (Figure 5a). Considering it is also generally difficult to pick the dispersion curve

in the low frequency range, this will probably be also true for the dispersion curve inversion. With the lower-frequency Love wave, however, the dispersion spectra inversion in the crossline case provides a more accurate result. The low-velocity layer is well recovered in the final model. This test indicates that the crossline acquisition system may provide better constraints at greater depth.

REAL DATA CASE

The synthetic tests shown above demonstrate the feasibility of using crossline data in surface-wave dispersion spectra inversion. Here we apply this method to a dataset collected at a geothermal site by the PoroTomo team. The site is located at Brady Hot Springs, Nevada where a ~8700-m fiber-optic cable is buried in shallow trenches (Feigl et al., 2017). The channel spacing is equal to 1-m and the gauge length is set to 10-m. The data were acquired by Silixa's iDAS[®] unit, which provides strain-rate records. The raw data have been converted to strain in this study. Several studies have been conducted to image the shallow structure at this site including active-source and passive-source DAS datasets. Parker et al. (2018) use arrivals on geophone and DAS records to build a V_p model at the top 250-m. Zeng et al. (2017b) use the NCFs of channel-pairs along one segment to avoid interference of Love wave and build fence-like pseudo 3D V_s structure.

Data from two types of sources are tested: active source and ambient noise. The active source signal is excited by a vibroseis truck with one vertical mode and two horizontal modes. We use records of one 70-m long cable segment for the horizontal

mode at two vibroseis points (Figure 6). The vibroseis truck excites swept-frequency signals which are removed via a cross-correlation method, as described in previous studies (Parker et al., 2018; Song et al., 2018). The noise cross-correlation function (NCF) between two receivers is extracted from the continuous ambient noise data, and the NCF can be used as an empirical Green's function for seismic tomography (e.g., Snieder and Wapenaar, 2010). The basic idea is to treat each receiver as a virtual source and the positive and negative lags of the NCF consist of the wave propagating between the two in one direction or the other. The ambient noise data are processed by a widely used approach (Zeng et al., 2017b). The virtual source is a channel in a parallel segment (Figure 6). Since the traffic on the highway next to the field site was the dominant noise source, we choose the negative lag of the noise cross-correlation functions for which the surface wave signal emerges clearly (Figure 7e).

A frequency-wavenumber filter is applied to suppress the body wave signal and other precursory noise. The minimum and maximum velocities are 100 m/s and 600 m/s, respectively. The processed records are shown in Figure 7a and 7c. The apparent velocity of the surface wave is about 260 m/s and its amplitude is much stronger than the body wave signal that has a velocity of about 800 m/s. The results of time-frequency analysis along the same channels indicate that the crossline data include a stronger high-frequency component. The high-frequency component is contributed by the Love wave signal that is lacking in the inline case.

The inversion results are obtained with the same search range for model 2 and they are shown in Figure 9. Obviously, the dispersion spectra of the three cases are more complicated than the

synthetic test ones. There are more jumps on the crossline data similar to the synthetic test (Figure 2). Since the shortest wavelength is about 10-m and the longest is about 40-m, we set up a layered model consisting of three layers over a half-space in which the top two layers are 5-m thick and the bottom layer is 10-m thick. The inverted models are generally consistent with each other, although there are some differences at the top 5 m. We also analyzed the records of a nearby geophone (Figure 6) for vibe point number 487. The time-frequency analysis pattern looks similar to the DAS record (Figure 8c). The Rayleigh wave signal around 0.5 s can be confirmed via the 90° phase shift between vertical and radial records (Figure 8a and 8b).

DISCUSSION

Gauge length, coupling, noise and topography

In practice, the gauge length setting affects the seismic signals. Theoretically, using a large gauge length could yield a better signal-to-noise ratio. However, this will come with a loss of spatial resolution and induce distortion of the high-frequency signals (Bakku, 2015; Dean et al., 2016; Shragge et al., 2019). Therefore, the optimal gauge length should be chosen according to the priori information of the site. The optimal gauge length is about half of the wavelength of the used signal (Dean et al., 2016). Previous study suggests the waveform will be distorted when the gauge length exceeds the wavelength, which means additional phase term is introduced. Since the phase difference across the array is used to compute the dispersion spectra in this study, such additional phase term of single channel's record will be cancelled. But this issue is still worth to be carefully investigated in the future.

The coupling between the cable and ground is assumed to be uniform in synthetic tests. The coupling did not show strong variations in our real case dataset (Figure 7a). Strong medium heterogeneity or contact force changes along a trench, conduit, or borehole may result in amplitude variations of DAS records. It is difficult to quantitatively calibrate the coupling with a repeating source (e.g., electric seismic source) in practice. To suppress such amplitude variations, trace normalization (e.g., root-mean-square normalization) can be introduced before stacking.

As is well known, the ambient noise source characteristics generally do not fully meet the theoretical assumptions. For example, an uneven source distribution introduces precursors (e.g., Zeng et al., 2017a). These non-ideal situations limit the signal quality of the surface wave in the NCF and its effect on the inversion result needs to be evaluated. We extracted a 2.0 s ambient noise record from the real dataset for each channel and normalized them with respect to the maximum value (Figure 10a). These noise records are dominated by the traffic on the highway next to the field site and the spectra indicate stronger noise between 7 Hz and 10 Hz. We added the normalized noise record to the crossline synthetic data (Figure 2c) with two noise levels, 10% and 20% (Figure 10c and 10d). The noise level is defined as the amplitude ratio between peak amplitudes of the noise and signal. The noise effect is more significant on the dispersion spectra (Figure 11) in the low-frequency band (7-11 Hz) than the high frequency band (> 15 Hz). One reason is the noise is stronger in the low frequency band (Figure 10b). The other factor is stronger scattering for high frequency noise, resulting in incoherent noise that is suppressed by the slant stack method. In the inverted models (Figure 11),

the shallow structure is not affected by the noise, whereas the deep part, which is constrained by the low frequency signal, is not well recovered in the 20% noise level case.

The other non-ideal case is a source located on a non-horizontal plane, such as a tilted base plate, or a topographic slope. In such a situation, the source can be expressed as a combination of vertical and horizontal single forces. We test the inversion with two dip angles. The relative amplitude of the vertical force is 18% in the 10° slope case and 26% for a 15° slope. As Figure 12 shows, the Rayleigh wave is affected by the slope. The effect of slope on the inverted model is weak for the top two layers, whereas the velocity of the half-space is not reliable when the slope is up to 15° (Figure 12). However, base-plate tilts up to 10° are rare in active source studies and large slopes are also not common for dark fiber-optic cable in cities, so this is likely not a significant issue in general.

Thickness, density and P-wave velocity

As in other surface wave inversion methods, our dispersion spectra inversion also needs to involve a small number of parameters, which is achieved in practice via fixed layer thickness and/or empirical relationships among P- and S-wave velocity, and density. Such simplifications are based on rule-of-thumb or a priori information which may break down in a real case (e.g., O'Neill, 2003; Bodet et al., 2005, 2009; Zywicki and Rix, 2005). We test the effects of varying layer thickness, density, and V_p with synthetic test model 1 (Table 1). In the following tests, the targeted parameter varies

through a specified range while the other parameters are kept fixed. The difference between the spectra of the true model and the perturbed model is computed.

The layer thickness is related to the size of the model space. Generally speaking, thin layers can fit data better. We discretize the model with 5-m and 2.5-m thick layers and invert the dispersion spectra (Figure 13). Since the input data include strong high frequency components, the thin layer model agrees well with the true model near the surface. However, more artificial jumps emerge in the 10-m to 30-m deep layer that are due to limited constraint at greater depth. It is better to use thin layers at shallow depth and test different layer thicknesses to analyze the trade-off between the number of parameters and fitting the data.

Since the surface wave is more sensitive to the S-wave velocity, in practice the P-wave velocity and density are derived from the S-wave velocity with a fixed ratio or an empirical relationship, which may introduce additional uncertainties. As Figure 14 shows, the effect of the density uncertainty on the total misfit is less than 5%. The most significant contribution is from the top two layers, which is about five times larger than that for the third layer and half-space. Therefore, inaccurate density will not bias the inversion result significantly.

The effect of P-wave velocity uncertainty is investigated with a similar approach. Figures 15a and 15b show the misfit increase for two cases. The first one is for unconsolidated sediments with a V_p/V_s ratio of about 4-9. In this case, the misfit increase is less than 1%, showing density's relatively weaker effect. The second case is for well consolidated rocks with a lower V_p/V_s ratio (~ 1.73). The V_p effect is up to

20%, which is not neglectable. The difference between these two cases can be explained based on the dispersion spectra difference. Figure 15c and 15d show two plots of the dispersion spectra at two particular frequency. When V_p/V_s is increased from 2 to 3, the root-mean-square difference at 10 Hz is approximately 14 times larger than that for V_p/V_s increasing from 4 to 5. In the consolidated case, V_p can be added to inversion and the recovered V_p model is reliable (Figure 16b). In the unconsolidated case, the V_p model is not well recovered. Other seismic tomography approaches (e.g., Konstantaki et al., 2013, Pasquet et al., 2015a; Pasquet et al., 2015b) can be used to construct a reliable V_p model from surface-wave inversion or joint inversion of P-wave reflection/refraction data and surface-wave data (e.g., Piatti et al., 2013).

CONCLUSION

DAS as a single-component “seismometer” provides dense spatial sampling that helps to record high frequency surface wave signals. In the crossline case, the DAS record consists of Rayleigh and Love waves, which cannot be separated into two distinct wave-trains in the time domain for separate dispersion measurements. We implement a surface-wave spectra dispersion inversion method that takes the two types of surface-wave signals into account. A series of synthetic tests verifies the reliability of our new method and suggests that the dispersion spectra inversion for crossline acquisition can jointly invert Rayleigh and Love waves and obtain a better model with the additional constraint. Our method is applied to both active source and ambient noise datasets acquired at a geothermal site and provides consistent inverted models with the

different datasets. Our method extends usable datasets and improves data constraints that can help to construct higher resolution models in practice.

ACKNOWLEDGMENTS

The data used in this study were acquired by the PoroTomo Team. The authors thank the PoroTomo team members for their hard work in the field. The authors thank four anonymous reviewers for their constructive comments that substantially improved the quality of this manuscript. This study is supported by the China National Natural Science Foundation under Grant 41974067 and the LU JIAXI International Team Program from the KC Wong Education Foundation and CAS (GJTD-2018-12)..

REFERENCES

- Ai, Z. Y., J. J. Mu, and G. P. Ren, 2018, 3D dynamic response of a transversely isotropic multilayered medium subjected to a moving load. *International Journal for Numerical and Analytical Methods in Geomechanics*, 42(4), 636-654.
- Ahmadi, S. F., and M. Eskandari, 2014, Vibration analysis of a rigid circular disk embedded in a transversely isotropic solid. *Journal of Engineering Mechanics*, 140(7), 04014048.
- Bakku, S. K., 2015, Fracture characterization from seismic measurements in a borehole, PhD thesis, Massachusetts Institute of Technology.
- Brocher, T. M., 2005, Empirical Relations between Elastic Wavespeeds and Density in

-
- the Earth's Crust. *Bulletin of the Seismological Society of America*, 95(6), 2081-2092.
- Bodet, L., K. van Wijk, A. Bitri, O. Abraham, P. Côte, G. Grandjean, and D. Leparoux, 2005, Surface-wave inversion limitations from laser-Doppler physical modeling. *Journal of Environmental & Engineering Geophysics*, 10(2), 151-162.
- Bodet, L., O. Abraham, and D. Clorennec, 2009, Near-offset effects on Rayleigh-wave dispersion measurements: Physical modeling. *Journal of Applied Geophysics*, 68(1), 95-103.
- Borcherdt, R. D., 1994, Estimates of site-dependent response spectra for design (methodology and justification). *Earthquake spectra*, 10, 617-617.
- Chipperfield, A., P. Fleming, H. Pohlheim, and C. Fonseca, 1994, Genetic algorithm toolbox for use with MATLAB.
- Dean, T., T. Cuny, and A. H. Hartog, 2016, The effect of gauge length on axially incident P - waves measured using fibre optic distributed vibration sensing. *Geophysical Prospecting*, 65(1), 184-193.
- Dou, S., and J. B. Ajo-Franklin, 2014, Full-wavefield inversion of surface waves for mapping embedded low-velocity zones in permafrost. *Geophysics*, 79(6), EN107-EN124.
- Dou, S., N. Lindsey, A. M. Wagner, T. M. Daley, B. Freifeld, M. Robertson, J. Peterson, C. Ulrich, E. R. Martin, and J. B. Ajo-Franklin, 2017, Distributed acoustic sensing for seismic monitoring of the near surface: A traffic-noise interferometry case study. *Scientific reports*, 7(1), 11620.

-
- Eskandari, M., S. F. Ahmadi, and S. Khazaeli, 2014, Dynamic analysis of a rigid circular foundation on a transversely isotropic half-space under a buried inclined time-harmonic load. *Soil Dynamics and Earthquake Engineering*, 63, 184-192.
- Eskandari, M., P. Samea, and S. F. Ahmadi, 2017, Axisymmetric time-harmonic response of a surface-stiffened transversely isotropic half-space. *Meccanica*, 52(1-2), 183-196.
- Feigl, K. L., and P. Team, 2017, Overview and preliminary results from the PoroTomo project at Brady Hot Springs, Nevada: Poroelastic tomography by adjoint inverse modeling of data from seismology, geodesy, and hydrology. In *Proceedings of the 42nd Workshop on Geothermal Reservoir Engineering*, Stanford, CA, USA (13-15).
- Forbriger, T., 2003, Inversion of shallow-seismic wavefields: I. Wavefield transformation. *Geophysical Journal International*, 153(3), 719-734.
- Foti, S., S. Parolai, D. Albarello, and M. Picozzi, 2011, Application of surface-wave methods for seismic site characterization. *Surveys in geophysics*, 32(6), 777-825.
- Henry, M., J. A. Orcutt, and R. L. Parker, 1980, A new method for slant stacking refraction data. *Geophysical Research Letters*, 7(12), 1073-1076.
- Herrmann, R. B., 2013, Computer programs in seismology: An evolving tool for instruction and research. *Seismological Research Letters*, 84(6), 1081-1088.
- Innanen, K. A., D. Lawton, K. Hall, K. L. Bertram, M. B. Bertram, and H. C. Bland, 2019, Design and deployment of a prototype multicomponent distributed acoustic sensing loop array. In *SEG Technical Program Expanded Abstracts 2019* (953-

957).

Konstantaki, L. A., S. Carpentier, F. Garofalo, P. Bergamo, and L. V. Socco, 2013, Determining hydrological and soil mechanical parameters from multichannel surface - wave analysis across the Alpine Fault at Inchbonnie, New Zealand. *Near Surface Geophysics*, 11(4), 435-448.

Kuvshinov, B. N., 2016, Interaction of helically wound fibre-optic cables with plane seismic waves. *Geophysical Prospecting*, 64(3), 671-688.

Li, Z., S. Ni, and P. Somerville, 2014, Resolving Shallow Shear-Wave Velocity Structure beneath Station CBN by Waveform Modeling of the Mw 5.8 Mineral, Virginia, Earthquake Sequence. *Bulletin of the Seismological Society of America*, 104(2), 944-952.

Lin, F., D. Li, R. W. Clayton, and D. Hollis, 2013, High-resolution 3D shallow crustal structure in Long Beach, California: Application of ambient noise tomography on a dense seismic array. *Geophysics*, 78(4), Q45-Q56.

Lindsey, N. J., E. R. Martin, D. S. Dreger, B. Freifeld, S. Cole, S. R. James, B. L. Biondi, and J. B. Ajo-Franklin, 2017, Fiber - optic network observations of earthquake wavefields. *Geophysical Research Letters*, 44(23), 11-792.

Lomax, A., and R. Snieder, 1994, Finding sets of acceptable solutions with a genetic algorithm with application to surface wave group dispersion in Europe. *Geophysical Research Letters*, 21(24), 2617-2620.

Ning, I. L. C., & P. Sava, 2018, High-resolution multi-component distributed acoustic sensing. *Geophysical Prospecting*, 66(6), 1111-1122.

-
- Maraschini, M., F. Ernst, S. Foti, and L. V. Socco, 2010, A new misfit function for multimodal inversion of surface waves. *Geophysics*, 75(4), G31-G43.
- Maraschini, M. and S. Foti, 2010, A Monte Carlo multimodal inversion of surface waves
- Mateeva, A., J. Lopez, D. Chalenski, M. Tatanova, P. Zwartjes, Z. Yang, S. Bakku, K. De Vos, and H. Potters, 2017, 4D DAS VSP as a tool for frequent seismic monitoring in deep water. *The Leading Edge*, 36(12), 995-1000.
- McMechan, G. A., and M. J. Yedlin, 1981, Analysis of dispersive waves by wave field transformation. *Geophysics*, 46(6), 869-874.
- O'Neill, A., 2003, Full-waveform reflectivity for modeling, inversion and appraisal of seismic surface wave dispersion in shallow site investigations. PHD thesis, University of Western Australia.
- Pan, Y., J. Xia, and C. Zeng, 2013, Verification of correctness of using real part of complex root as Rayleigh-wave phase velocity with synthetic data. *Journal of Applied Geophysics*, 88, 94-100.
- Park, C. B., R. D. Miller, and J. Xia, 1999, Multichannel analysis of surface waves. *Geophysics*, 64(3), 800-808.
- Parker, L. M., C. H. Thurber, X. Zeng, P. Li, N. E. Lord, D. Fratta, H. F. Wang, M. C. Robertson, A. M. Thomas, M. S. Karplus, A. Nayak, and K. L. Feigl, 2018, Active-source seismic tomography at the Brady Geothermal Field, Nevada, with dense nodal and fiber-optic seismic arrays. *Seismological Research Letters*, 89(5), 1629-1640.

-
- Parker, T. R., S. V. Shatalin, and M. Farhadiroushan, 2014, Distributed Acoustic Sensing-a new tool for seismic applications. *First Break*, 32(2), 61-69.
- Pasquet, S., L. Bodet, A. Dhemaied, A. Mouhri, Q. Vitale, F. Rejiba, N. Flipo, and R. Guérin, 2015a, Detecting different water table levels in a shallow aquifer with combined P-, surface and SH-wave surveys: Insights from VP/VS or Poisson's ratios. *Journal of Applied Geophysics*, 113, 38-50.
- Pasquet, S., L. Bodet, L. Longuevergne, A. Dhemaied, C. Camerlynck, F. Rejiba, and R. Guerin, 2015b, 2D characterization of near-surface VP/VS: surface - wave dispersion inversion versus refraction tomography. *Near Surface Geophysics*, 13(4), 315-332.
- Piatti, C., L. V. Socco, D. Boiero, and S. Foti, 2013, Constrained 1D joint inversion of seismic surface waves and P-refraction traveltimes. *Geophysical Prospecting*, 61, 77-93.
- Rix, G. J., and E. A. Leipski, 1991, Accuracy and resolution of surface wave inversion. recent advances in instrumentation, data acquisition and testing in soil dynamics. proceedings of sessions sponsored by the geotechnical engineering division of the american society of civil engineers inc. Publication of American Society of Civil Engineers.
- Ryden, N., and C. B. Park, 2006, Fast simulated annealing inversion of surface waves on pavement using phase-velocity spectra. *Geophysics*, 71(4), R49-R58.
- Shragge, J., J. Yang, Issa, N. A. Issa, M. Roelens, M. Dentith, and S. Schediwy, 2019, Low-frequency ambient Distributed Acoustic Sensing (DAS): Useful for

-
- subsurface investigation? In SEG Technical Program Expanded Abstracts 2019 (963-967).
- Snieder, R., and K. Wapenaar, 2010, Imaging with ambient noise. *Physics Today*, 63(9), 44-49.
- Song, Z., X. Zeng, C. H. Thurber, H. F. Wang, and D. Fratta, 2018, Imaging shallow structure with active-source surface wave signal recorded by distributed acoustic sensing arrays. *Earthquake Science*, 31, 208-214.
- Xia, J., R. D. Miller, and C. B. Park, 1999, Estimation of near-surface shear-wave velocity by inversion of Rayleigh waves. *Geophysics*, 64(3), 691-700.
- Zeng, X., C. Lancelle, C. H. Thurber, D. Fratta, H. F. Wang, N. Lord, and A. Clarke, 2017a, Properties of noise cross-correlation functions obtained from a distributed acoustic sensing array at Garner Valley, California. *Bulletin of the Seismological Society of America*, 107(2), 603-610.
- Zeng, X., C. H. Thurber, H. F. Wang, and D. Fratta, 2017b, 3D shear wave velocity structure revealed with ambient noise tomography on a DAS array. In AGU Fall Meeting Abstracts.
- Zhan, Z., 2020, Distributed Acoustic Sensing Turns Fiber-Optic Cables into Sensitive Seismic Antennas. *Seismological Research Letters*, 91(1), 1-15.
- Zywicki, D. J., and G. J. Rix, 2005, Mitigation of near-field effects for seismic surface wave velocity estimation with cylindrical beamformers. *Journal of Geotechnical & Geoenvironmental Engineering*, 131(8), 970-977.

FIGURES

Figure 1. Different acquisition configurations and their effects on seismic recordings.

(a) inline; (b) crossline. The star represents the source and the black arrow shows the direction of source excitation. The circles are receiver channels on the cable. (c) DAS synthetic records of the inline (solid line) and crossline (dashed line) cases.

Figure 2. The synthetic records and dispersion spectra of the inline and crossline cases.

(a) Synthetic records of the inline case (all the traces shown as color image, selected records shown as black lines); (b) surface wave dispersion spectrum of the inline case; (c) and (d) are the same for the crossline case. The dashed lines in (a) and (c) denote the arrival time for a velocity of 250 m/s (gray) and 500 m/s (black). The theoretical dispersion curves of Rayleigh and Love waves are indicated by the solid and dashed lines, respectively in (b) and (d), whereas the maximum stacking energy points are shown by black crosses.

Figure 3. Results of the dispersion curve and spectra inversion methods.

(a) The initial models (light gray), true model (dark gray) and final models (gray dash: dispersion curve and black: dispersion spectra). (b) and (c) are observed and theoretical amplitude normalized dispersion spectra, respectively. The 90% energy picking errorbar are shown in black and the gray line is the dispersion curve. (d) Dispersion curve fitting result. (e) The surface wave spectra normalized amplitude residuals.

Figure 4. Results of the dispersion spectra inversion method for the crossline case.

(a) The initial models (light gray), true model (dark gray) and final model (black). (b) The amplitude-normalized theoretical dispersion spectra. (c) The amplitude-normalized residuals of the dispersion spectra method.

Figure 5. Results of the dispersion spectra inversion method for the model with a low velocity layer.

(a) The initial models (light gray), true model (dark gray) and final models (gray dash: inline case and black: crossline case). (b-d) Amplitude-normalized observed and theoretical dispersion spectra and the residuals in the inline case, respectively. (e-g) same as (b-d) for the crossline case.

Figure 6. Location map of the cable and source from the PoroTomo project.

The gray line is the part of the cable selected for this study, and the asterisks indicate the sources. The virtual source is at ch260. The black arrow indicates the direction of the source. The black cross indicates the geophone. 487 and 496 are PoroTomo vibe point numbers, inline and crossline, respectively. N132 is a three-component short-period geophone.

Figure 7. Waveform and time-frequency analysis (gray line) in the case of (a and b) inline, (c and d) crossline active source and (e and f) crossline NCF.

Figure 8. Geophone records and time-frequency analysis.

(a) Time series of the vertical and radial components. (b) The phase of the vertical component record has been shifted by 90° via Hilbert transform. (c) The time-frequency analysis of the vertical component record shown in (a). The time window indicated by the dashed line denotes the Rayleigh

wave signals with a clear 90° phase difference between the vertical and radial components.

Figure 9. The inversion results of the PoroTomo dataset.

(a) Velocity model, where the black line is the inline case, the light gray line is the crossline case and the dark gray line is the velocity structure from ambient noise. (b-d) Amplitude-normalized observed and theoretical dispersion spectra and the residuals in the inline case, respectively. (e-g) same as (b-d) for the crossline case. (h-j) Corresponding result for the ambient noise case.

Figure 10. Synthetic data with noise example.

(a) The noise extracted from the real dataset; (b) spectral of normalized noise and normalized synthetic records; (c) synthetic record with 10% noise; (d) synthetic record with 20% noise.

Figure 11. The inversion results for the noise example.

(a) The true model (light gray) and final models (dark gray: 10% noise and black: 20% noise). (b-d) Normalized observed dispersion spectra, the normalized theoretical dispersion spectra, and the residual in the inline case, respectively. (e-g) same as (b-d) for the crossline case.

Figure 12. Synthetic waveforms and inversion results for the slope example.

(a) The true model (light gray) and final models (dark gray: 10° and black: 15°). (b) Waveforms with different slopes (black: 0° ; dark gray: 10° ; light gray: 15°). (c) Amplitude-normalized observed dispersion spectra for the 10° case. (d) The difference between the observed dispersion spectra between the 10° case and 15° case.

Figure 13. The effect of layer thickness on the inversion results.

(a) The true model (light gray) and final models (dark gray: thickness equal to 5-m and black: 2.5-m). (b-d) The amplitude-normalized observed and theoretical dispersion spectra, and the residual for 5-m layer thickness. (e-g) The case for 2.5-m layer thickness.

Figure 14. Contribution of density to the misfit function.

Line denotes misfit increase due to error in the density of each layer. Model 1 is used as the reference model.

Figure 15. Influence of V_p variation on the inversion results.

(a) V_p is calculated according to an empirical formula (unconsolidated case, V_p/V_s range from 4 to 6); (b) V_p is calculated assuming a Poisson solid (consolidated case, $V_p/V_s=1.73$); (c-d) Amplitude-normalized plots of the spectra at 10 Hz and 20 Hz, respectively.

Figure 16. Simultaneous inversion of S-wave and P-wave velocity using the dispersion spectra inversion method.

(a) S-wave velocity structure, (b) P-wave velocity structure of consolidated sediments, and (c) P-wave velocity structure of unconsolidated sediments. The search ranges for V_p are shown as the dash gray lines.

TABLE

Table 1. Velocity models for the synthetic tests

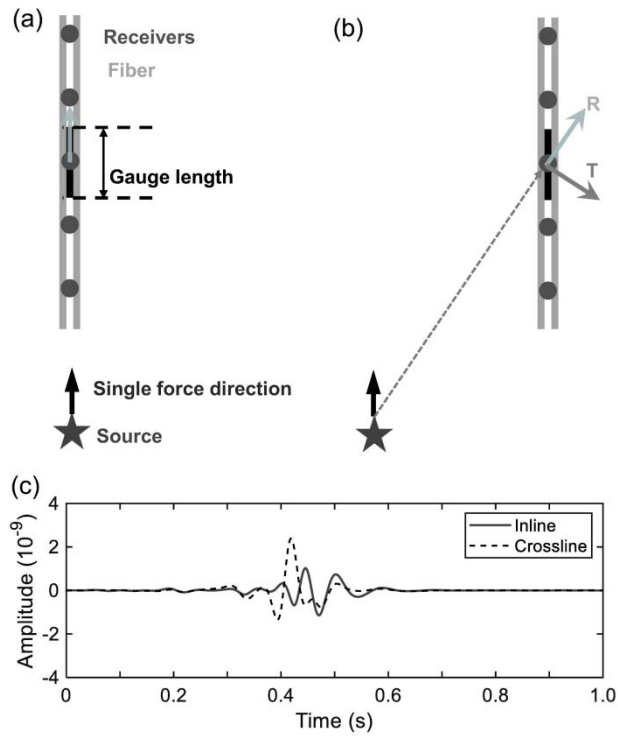


Figure 1. Different acquisition configurations and their effects on seismic recordings. (a) inline; (b) crossline. The star represents the source and the arrow shows the direction of source excitation. The circles are receiver channels on the cable. (c) DAS synthetic records of the inline (solid line) and crossline (dashed line) cases.

254x190mm (300 x 300 DPI)

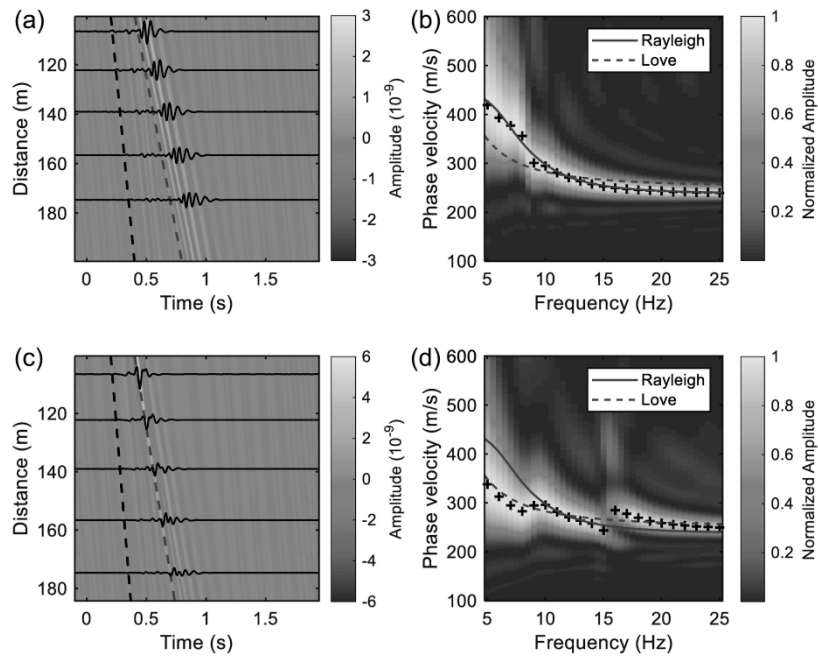


Figure 2. The synthetic records and dispersion spectra of the inline and crossline cases. a) Synthetic records of the inline case (all the traces shown as color image, selected records shown as black lines); (b) surface wave dispersion spectrum of the inline case; (c) and (d) are the same for the crossline case. The dashed lines in (a) and (c) denote the arrival time for a velocity of 250 (gray) and 500 m/s (black). The theoretical dispersion curves of Rayleigh and Love waves are indicated by the solid and dashed lines, respectively in (b) and (d), whereas the maximum stacking energy points are shown by black crosses.

254x190mm (300 x 300 DPI)

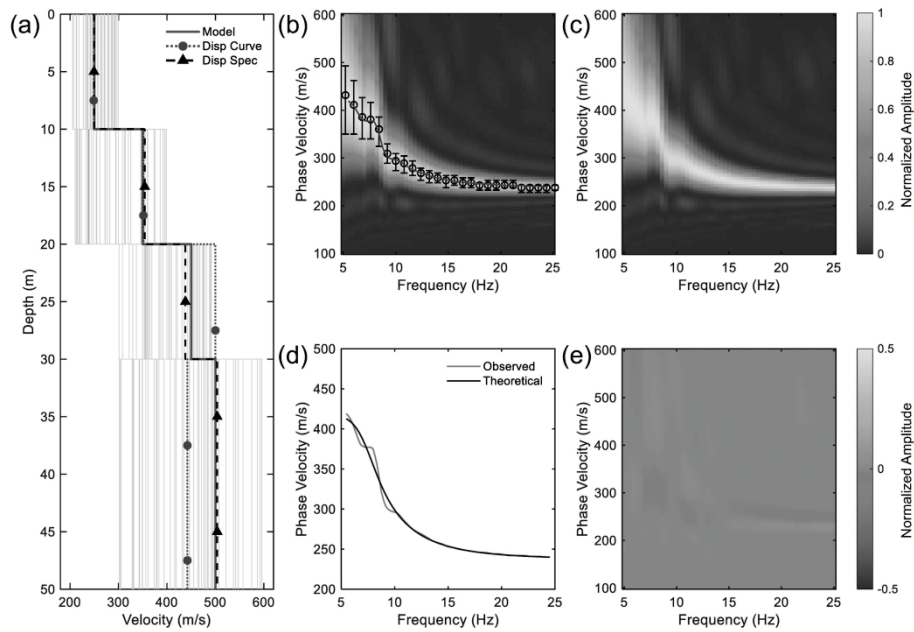


Figure 3. Results of the dispersion curve and spectra inversion methods.
 a) The initial models (light gray), true model (dark gray) and final models (gray dash: dispersion curve and black: dispersion spectra). (b) and (c) are observed and theoretical amplitude normalized dispersion spectra, respectively. The 90% energy picking errorbar are shown in black and the gray line is the dispersion curve. (d) Dispersion curve fitting result. (e) The surface wave spectra normalized amplitude residuals.

254x190mm (300 x 300 DPI)

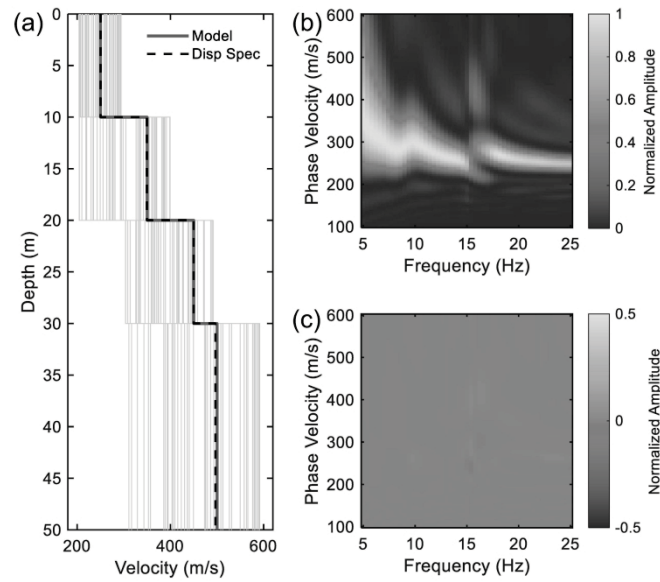


Figure 4. Results of the dispersion spectra inversion method for the crossline case. (a) The initial models (light gray), true model (dark gray) and final model (black). (b) The amplitude-normalized theoretical dispersion spectra. (c) The amplitude-normalized residuals of the dispersion spectra method.

254x190mm (300 x 300 DPI)

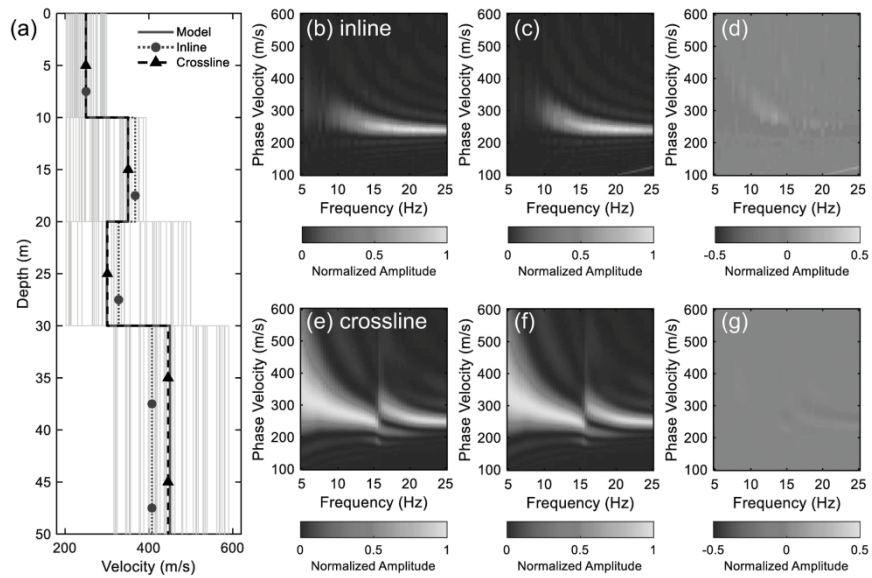


Figure 5. Results of the dispersion spectra inversion method for the model with a low velocity layer. (a) The initial models (light gray), true model (dark gray) and final models (gray dash: inline case and black: crossline case). (b-d) Amplitude-normalized observed and theoretical dispersion spectra and the residuals in the inline case, respectively. (e-g) same as (b-d) for the crossline case.

254x190mm (300 x 300 DPI)

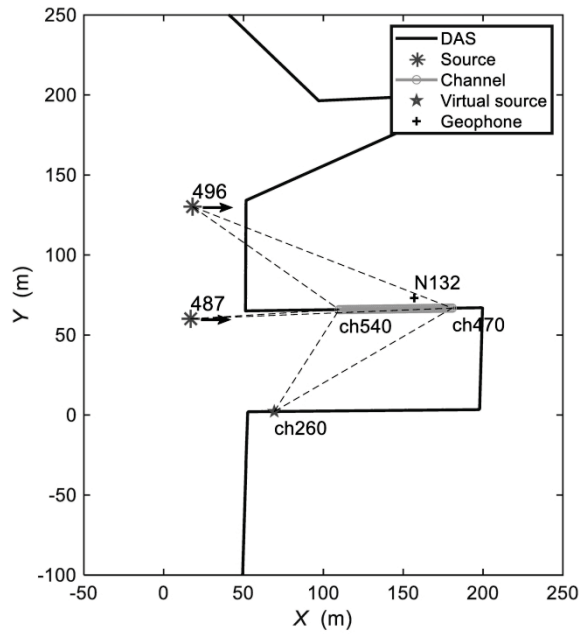


Figure 6. Location map of the cable and source from the PoroTomo project. The gray line is the part of the cable selected for this study, and the asterisks indicate the sources. The virtual source is at ch260. The black arrow indicates the direction of the source. The black cross indicates the geophone. 487 and 496 are PoroTomo vibe point numbers, inline and crossline, respectively. N132 is a three-component short-period geophone.

253x195mm (300 x 300 DPI)

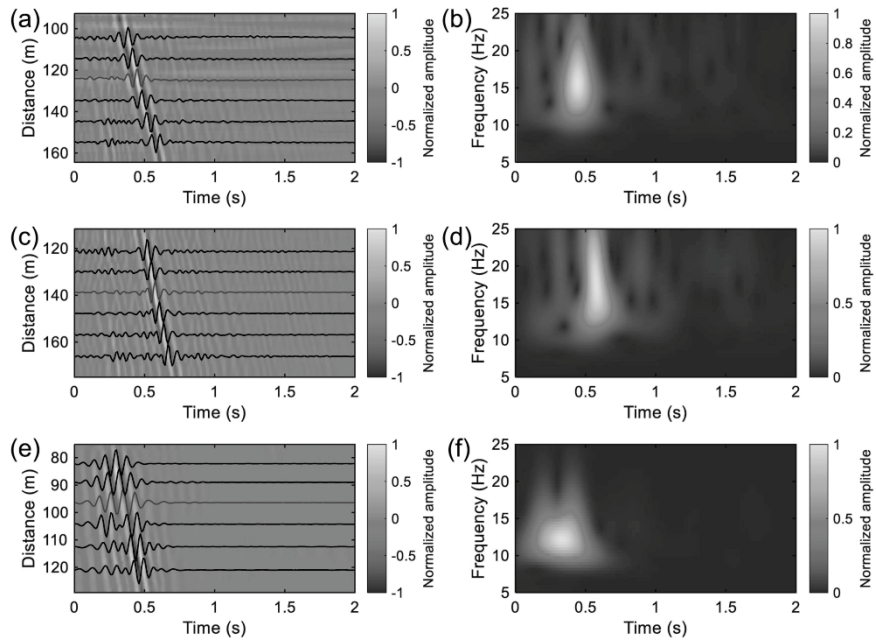


Figure 7. Waveform and time-frequency analysis (gray line) in the case of (a and b) inline, (c and d) crossline active source and (e and f) crossline NCF.

254x190mm (300 x 300 DPI)

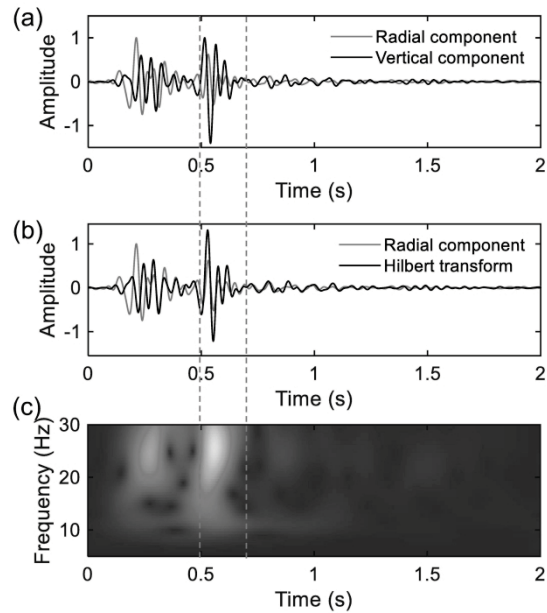


Figure 8. Geophone records and time-frequency analysis.

(a) Time series of the vertical and radial components. (b) The phase of the vertical component record has been shifted by 90° via Hilbert transform. (c) The time-frequency analysis of the vertical component record shown in (a). The time window indicated by the dashed line denotes the Rayleigh wave signals with a clear 90° phase difference between the vertical and radial components.

254x190mm (300 x 300 DPI)

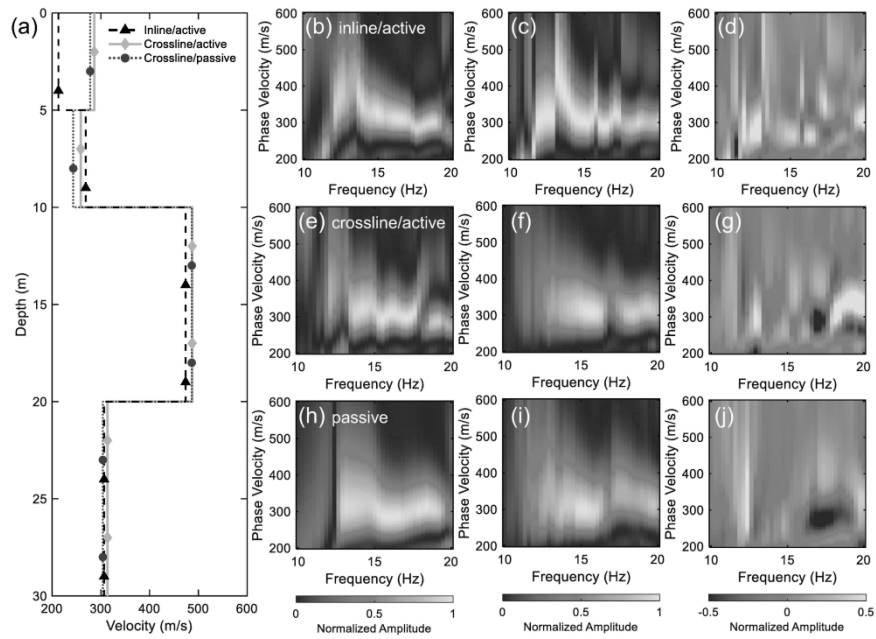


Figure 9. The inversion results of the PoroTomo dataset.

(a) Velocity model, where the black line is the inline case, the light gray line is the crossline case and the dark gray line is the velocity structure from ambient noise. (b-d) Amplitude-normalized observed and theoretical dispersion spectra and the residuals in the inline case, respectively. (e-g) same as (b-d) for the crossline case. (h-j) Corresponding result for the ambient noise case.

254x190mm (300 x 300 DPI)

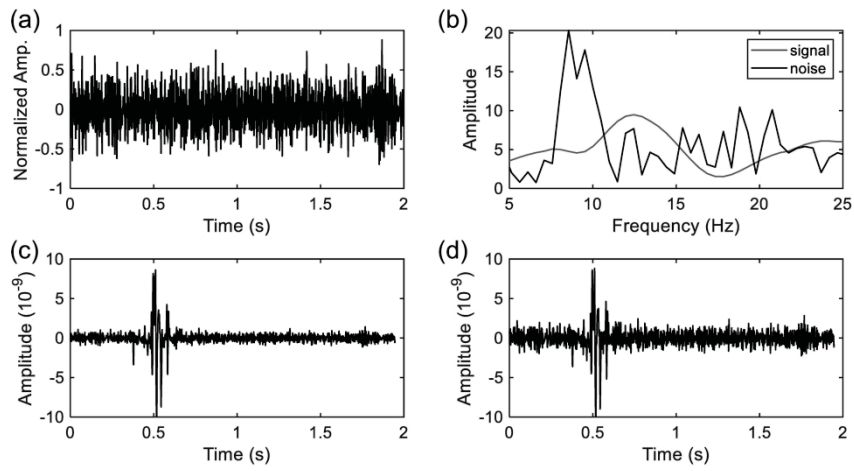


Figure 10. Synthetic data with noise example.
 (a)The noise extracted from the real dataset; (b) spectral of normalized noise and normalized synthetic records; (c) synthetic record with 10% noise;(d) synthetic record with 20% noise.

254x190mm (300 x 300 DPI)

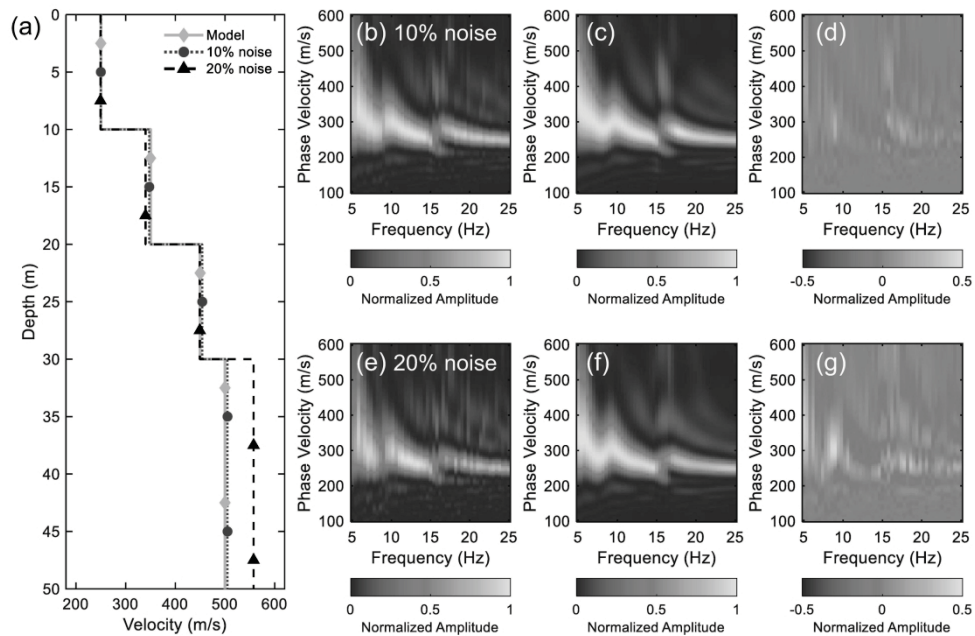


Figure 11. The inversion results for the noise example.

(a) The true model (light gray) and final models (dark gray: 10% noise and black: 20% noise). (b-d) Normalized observed dispersion spectra, the normalized theoretical dispersion spectra, and the residual in the inline case, respectively. (e-g) same as (b-d) for the crossline case.

254x190mm (300 x 300 DPI)

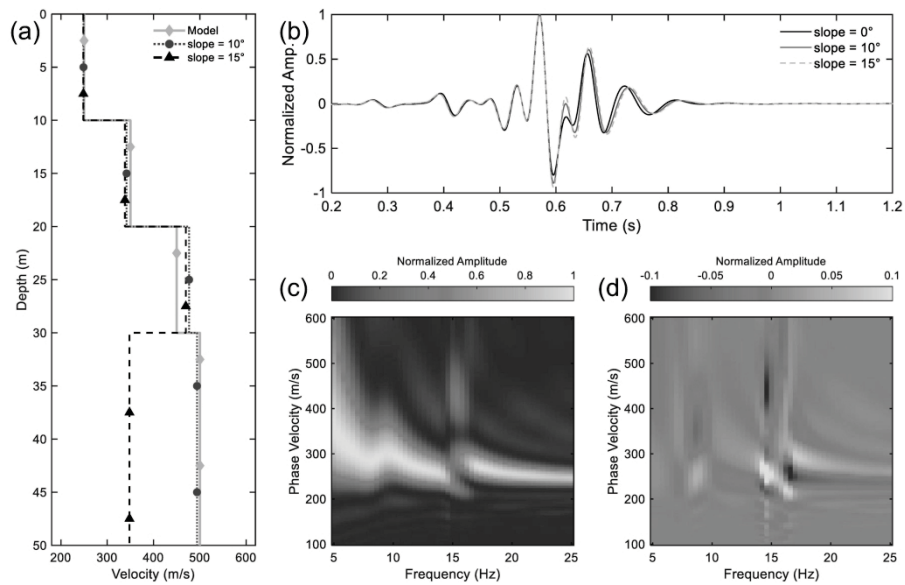


Figure 12. Synthetic waveforms and inversion results for the slope example.
 (a) The true model (light gray) and final models (dark gray: 10° and black: 15°). (b) Waveforms with different slopes (black: 0 degrees; dark gray: 10 degrees; light gray: 15 degrees). (c) Amplitude-normalized observed dispersion spectra for the 10° case. (d) The difference between the observed dispersion spectra between the 10° case and 15° case.

254x190mm (300 x 300 DPI)

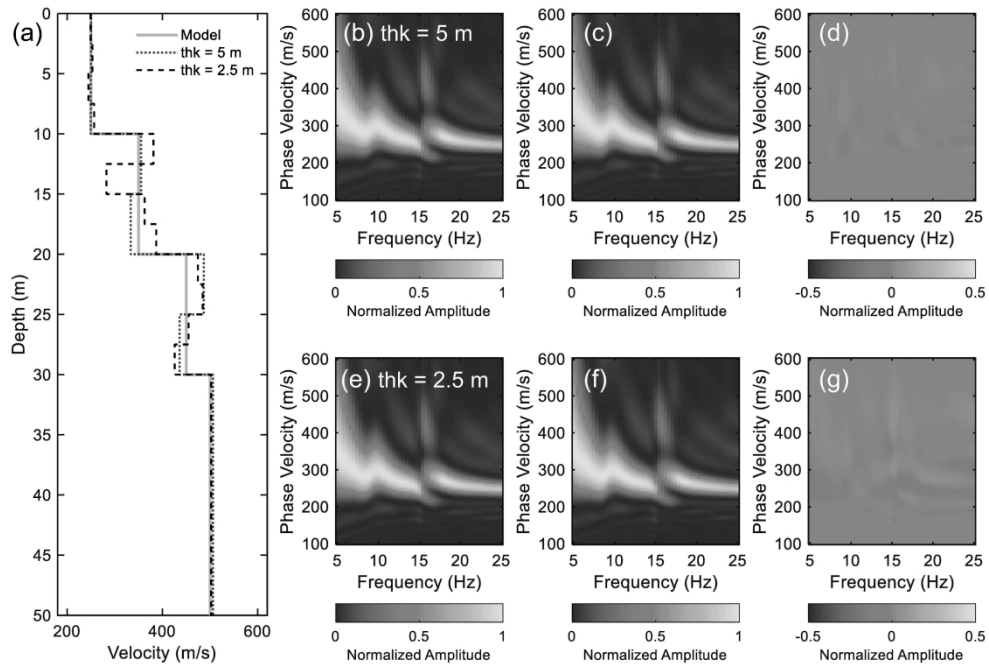


Figure 13. The effect of layer thickness on the inversion results.
 a) The true model (light gray) and final models (dark gray: thickness equal to 5-m and black: 2.5-m). (b-d) The amplitude-normalized observed and theoretical dispersion spectra, and the residual for 5-m layer thickness. (e-g) The case for 2.5-m layer thickness.

254x190mm (300 x 300 DPI)

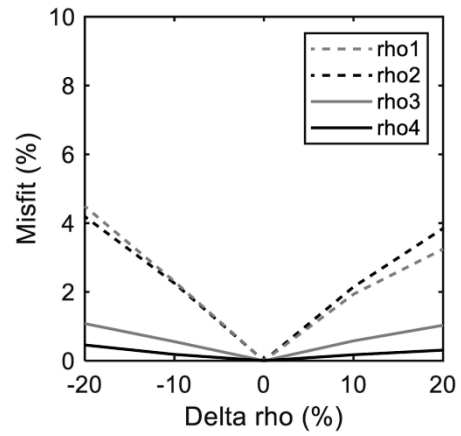


Figure 14. Contribution of density to the misfit function. Line denotes misfit increase due to error in the density of each layer. Model 1 is used as the reference model.

254x190mm (300 x 300 DPI)

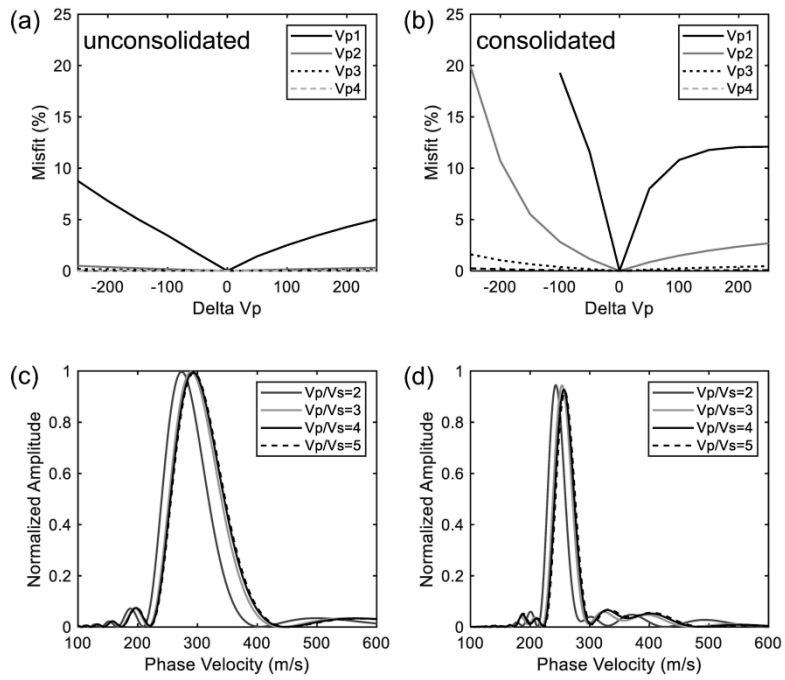


Figure 15. Influence of V_p variation on the inversion results. (a) V_p is calculated according to an empirical formula (unconsolidated case, V_p/V_s range from 4 to 6); (b) V_p is calculated assuming a Poisson solid (consolidated case, $V_p/V_s=1.73$); (c-d) Amplitude-normalized plots of the spectra at 10 Hz and 20 Hz, respectively.

254x190mm (300 x 300 DPI)

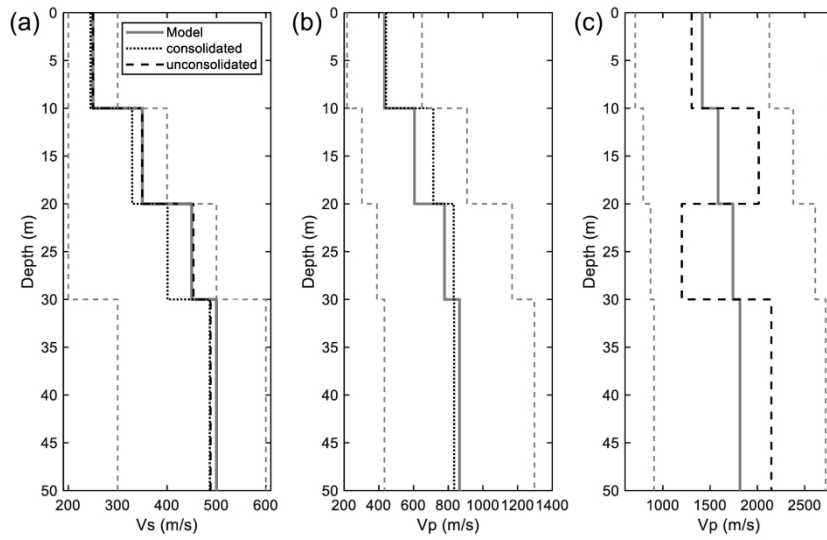


Figure 16. Simultaneous inversion of S-wave and P-wave velocity using the dispersion spectra inversion method.

(a) S-wave velocity structure, (b) P-wave velocity structure of consolidated sediments, and (c) P-wave velocity structure of unconsolidated sediments. The search ranges for Vp are shown as the dash gray lines.

254x190mm (300 x 300 DPI)

Table 1

del index	layer index	Thickness (m)	Vs (m/s)	Vs search range (m/s)
1	1	10	250	[200, 300]
	2	10	350	[200, 400]
	3	10	450	[300, 500]
	4	/	500	[300, 600]
2	1	10	250	[200, 300]
	2	10	350	[200, 400]
	3	10	300	[200, 500]
	4	/	450	[300, 600]

m/s	Density (g/cm ³)
17	1.90
85	1.95
41	2.00
15	2.02
17	1.90
85	1.95
03	1.93
41	2.00

AD MATERIALS AVAILABILITY

Materials associated with this research are available and can be obtained by contacting the corresponding author.